Composite level approach to the hyperfine structure of the sodium $D1$ transition

R. S. Gurjar and K. K. Sharma
Department of Physics and Centre for Laser Technology, Indian Institute of Technology, Kanpur 208 016, India
(Received 8 May 1995; revised manuscript received 8 September 1995)

Population changes among the hyperfine levels of the sodium $D1$ transition, created by a weakly saturating narrow-band pump, are detected by a counterpropagating probe in a 10-cm-long cell containing sodium vapor without any buffer gas. All Lamb dips and cross over resonances with linewidths approaching natural widths are clearly resolved. We have applied a five composite level model to interpret the observed probe absorption. The rate equations were solved analytically. The model predicts specific relationships between the frequency integrated probe absorption coefficient of crossover and Lamb dip resonances. We find excellent agreement in the case of crossover resonances that involve a single ground-state hyperfine level. The agreement is not so good for crossover resonances for which both ground hyperfine levels participate.

PACS number(s): 33.80.Be, 32.30.−r, 32.70.Jz

I. INTRODUCTION

A number of high-resolution spectroscopic techniques in the frequency domain, such as saturation spectroscopy, polarization spectroscopy, and velocity-selective optical pumping, have emerged in recent years to probe optical transitions in atomic and molecular systems [1–3]. This has become possible with the availabilty of commercial narrow-band single-mode dye lasers. Sodium is a classic example of atomic spectroscopy. Hänsch *et al.* [1] used dye lasers for the high-resolution spectroscopy of sodium. Counterpropagating pump and probe pulses obtained from a nitrogen laser pumped dye laser were made to pass through a 10-cm-long cell containing sodium at 110 °C. With 7-MHz bandwidth laser pulses, they were able to resolve the hyperfine structure of the sodium $D1$ line. The narrowest spectral line in their measurement had a full width at half maximum (FWHM) of 40 MHz. The role of velocity-changing collisions (VCC's) in optical pumping of Na vapor was studied by Pappas and co-workers [4]. In the absence of VCC's, only a small fraction of the Na atoms out of the full Doppler profile can interact with the narrow-band laser and get oriented. An oriented Na atom undergoing VCC's with the spherically symmetric argon atom remains oriented, although it may no longer be resonant with the laser radiation. However, the nonresonant Na atoms after VCC's may change their velocities and become resonant and in turn get oriented. Thus the sample polarization spreads over the entire Doppler profile. These authors observed more than 90% polarization at the argon buffer gas pressure in the neighborhood of 200 mTorr. The observed structure was not entirely Doppler-free and they used a four-level model to interpret their experimental results. Quivers [5] developed composite-level theoretical models within the rate equation approximation but including VCC effects to describe optical pumping in multilevel transitions. Svanberg *et al.* [6], with a 1-MHz bandwidth cw dye laser, obtained Doppler-free spectrum of sodium D lines under conditions of strong pump and high integrated sample absorption (the cell length was 30 cm). Subnatural linewidths for the crossover resonances were reported by these authors. They observed that in optically thick samples, the wings in the Doppler profile are strongly absorbed, leading to essentially background-free narrow resonances. Recently, Shimkaveg and co-workers [7] applied Quivers's four-level model to the $D1$ line in ^{6}Li where the hyperfine structure of the excited state remained unresolved. However, for the sodium $D1$ line, with the fully resolved hyperfine structure of both the terminal states, a five-level model has to be used. In this paper we report the Doppler-free spectrum of the sodium $D1$ line obtained from a 10-cm long vapor cell at various temperatures. The five-level model has been applied to interpret the experimental results. Our experimental observations are in good agreement with certain predictions of the five-level model.

II. FIVE-LEVEL MODEL

The hyperfine structure of the $D1$ line of ^{23}Na is shown in Fig. 1(a). The ground state $3\,^2S_{1/2}$ and the excited state $3\,^2P_{1/2}$ are each split into hyperfine (hf) pairs ($F=1$, $F=2$) with 1772-MHz and 189-MHz separations, respectively. The hf splittings of both levels are large enough to be well resolved in our experiment. As in Ref. [5], the 16 magnetic sublevels of $^2S_{1/2}$ and $^2P_{1/2}$ can be grouped into 6 composite

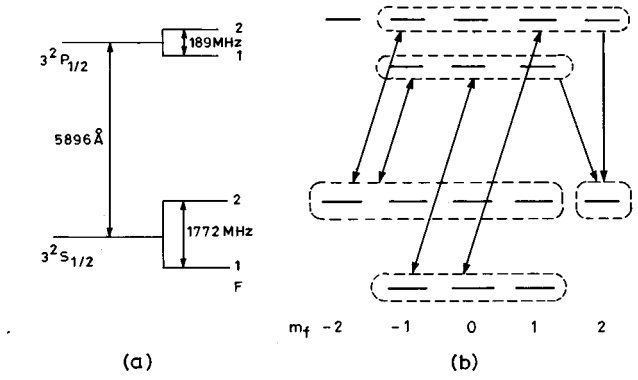

FIG. 1. (a) Hyperfine structure of the $D1$ line of ^{23}Na. Double arrows in (b) represent laser-induced transitions, while single arrows represent spontaneous emission. Other spontaneous transitions are not shown in the figure. The sublevels are grouped as indicated by the broken lines. Pumping is with right circularly polarized light.

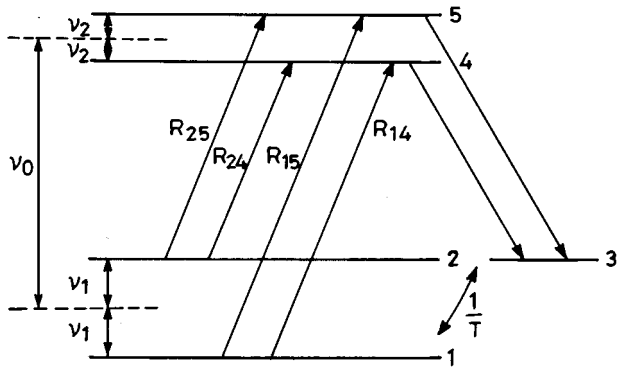

FIG. 2. Composite five-level model for the $D1$ line of sodium. R_{ij} are the pumping rates. Spontaneous emissions from levels 4 and 5 to levels 1 and 2 are not shown. T is the time in which populations of the levels 1, 2, and 3 reach thermal equilibrium.

levels if right circularly polarized light, which causes only $\Delta m=+1$ transitions is used to excite the $D1$ line [Fig. 1(b)]. In this model, all magnetic sublevels (belonging to a given hf level) with equal populations are grouped into a single composite level. The composite level 3 belonging to the $^2S_{1/2}$ state with $F=2$, $m_f=+2$ does not participate in the absorption process and so is distinguished from level 2 with $F=2$, $m_f=-2,-1,0,1$. The composite level 6 belonging to the $^2P_{1/2}$ with $F=2$ and $m_f=-2$ does not participate in the whole process and is therefore ignored. We effectively have five composite levels to deal with (Fig. 2). Further, we use a rate equation approach to describe the dynamics of the level populations because it provides analytical results that can be put to direct experimental tests. We will return to this point in Sec. IV. Because of the complexity of the five-level model, we did not use a buffer gas in the present study so that the model can be tested in the absence of complications due to collisions with the buffer gas. Further, the Na vapor density is sufficiently low to eliminate Na-Na collisions. The relevant rate equations are written as

$$\dot{N}_1=-\left[\frac{N_1}{3}-\frac{N_4}{3}\right]R_{14}-\left[\frac{N_1}{3}-\frac{N_5}{4}\right]R_{15}+\Gamma_{51}N_5+\Gamma_{41}N_4-\frac{[N_1-N_1^0]}{T}, \tag{1}$$

$$\dot{N}_2=-\left[\frac{N_2}{4}-\frac{N_4}{3}\right]R_{24}-\left[\frac{N_2}{4}-\frac{N_5}{4}\right]R_{25}+\Gamma_{52}N_5+\Gamma_{42}N_4-\frac{[N_2-N_2^0]}{T}, \tag{2}$$

$$\dot{N}_4=-\left[\frac{N_4}{3}-\frac{N_1}{3}\right]R_{14}-\left[\frac{N_4}{3}-\frac{N_2}{4}\right]R_{24}-\left[\frac{1}{T}+\frac{1}{\tau}\right]N_4, \tag{3}$$

$$\dot{N}_5=-\left[\frac{N_5}{4}-\frac{N_1}{3}\right]R_{15}-\left[\frac{N_5}{4}-\frac{N_2}{4}\right]R_{25}-\left[\frac{1}{T}+\frac{1}{\tau}\right]N_5, \tag{4}$$

TABLE I. Relevant cross sections and decay rates for the $D1$ transition.

Transition i-j	σ_{ij} [units of $\pi\lambda^2(\gamma_N/\gamma_H)$][a]	Γ_{ji}[b] (units of $\frac{1}{\tau}$)
1-4	1/3	1/6
1-5	5/3	1/2
2-4	5/3	2/3
2-5	5/3	3/8
3-4	0	1/6
3-5	0	1/8

[a] γ_N/γ_H is the ratio of the natural to the homogeneous linewidth.
[b] τ is the radiative lifetime of the $3\,^2P_{1/2}$ state.

$$\dot{N}_3=+\Gamma_{43}N_4+\Gamma_{53}N_5-\frac{[N_3-N_3^0]}{T}. \tag{5}$$

Here

$$R_{ij}=\left(\frac{\sigma_{ij}I}{h\nu}\right)\frac{(\gamma_H/2)^2}{(\Delta_{ij}-x)^2+(\gamma_H/2)^2} \tag{6}$$

represents the pumping rate from the composite levels $i=1,2$ to the composite levels $j=4,5$ and the homogeneous absorption cross sections σ_{ij} are listed in Table I. The homogeneous linewidth $\gamma_H=1/\tau+2/T$; Δ_{ij} is the detuning of the laser frequency ω from the transition frequency ω_{ij}; $x=2\pi v/\lambda$, where v is the axial atomic velocity; I is the pump laser intensity. The spontaneous lifetimes of levels 4 and 5 are taken to be the same (τ); the spontaneous decay rates (Γ_{ji}) between pairs of levels are also listed in Table I. The pump-created population changes in the levels are assumed to relax to their equilibrium values with a relaxation time T, which is also taken to be the same for all levels. In the present case, the relaxation time is simply the beam passage time of the atoms. Using the general procedure outlined in Ref [5], the steady-state level populations can be expressed as

$$N_1=N_1^0+S_{14}^1\mathscr{L}'_{14}+S_{15}^1\mathscr{L}'_{15}+S_{24}^1\mathscr{L}'_{24}+S_{25}^1\mathscr{L}'_{25}, \tag{7}$$

$$N_2=N_2^0+S_{14}^2\mathscr{L}'_{14}+S_{15}^2\mathscr{L}'_{15}+S_{24}^2\mathscr{L}'_{24}+S_{25}^2\mathscr{L}'_{25}, \tag{8}$$

$$N_4=S_{14}^4\mathscr{L}'_{14}+S_{24}^4\mathscr{L}'_{24}, \tag{9}$$

$$N_5=S_{15}^5\mathscr{L}'_{15}+S_{25}^5\mathscr{L}'_{25}, \tag{10}$$

where

$$\mathscr{L}'_{ij}=\frac{(\gamma_H/2)^2}{(\Delta_{ij}-x)^2+(1+S_{ij})(\gamma_H/2)^2} \tag{11}$$

and S_{ij} and S_{ij}^k are defined in the Appendix.

III. PROBE TRANSMISSION

It should be understood that the narrow-band ($\sim$1 MHz) pump of frequency ν interacts with a particular velocity

group of atoms. So the populations N_i and N_i^0 of the ith level appearing in the above equations actually represent velocity-dependent populations $N_i(x)$ and $N_i^0(x)$, respectively. Here $N_i^0(x)=N_{i,0}G(x)$, where $N_{i,0}$ is the total number of atoms at thermal equilibrium in the ith level and $G(x)$ represents the normalized Gaussian distribution $(1/\sqrt{\pi}ku)e^{-(x/ku)^2}$, where u is the most probable velocity. Expressions (7)–(10) give the redistribution of level populations for a particular velocity group caused by a σ^+-polarized pump of intensity I. The population changes monitored by a weak counterpropagating (or copropagating) probe having the frequency and polarization of the pump are, however, not velocity sensitive because the laser at a given frequency interacts with all velocity groups lying within the homogeneous width of the transition. The measured change in the probe absorption at a particular setting of the laser frequency takes into account contributions from all such velocity groups. The narrow homogeneous profile ($\sim$ 10 MHz) ensures, however, that the contributions from the distant velocity groups are indeed insignificant. The velocity-integrated probe absorption coefficient can be written as

$$\alpha_{\text{probe}}=\int (N_1-N_4)\bar{\sigma}_{14}dx+\int (N_1-N_5)\bar{\sigma}_{15}dx + \int (N_2-N_4)\bar{\sigma}_{24}dx+\int (N_2-N_5)\bar{\sigma}_{25}dx. \tag{12}$$

Here the average absorption cross section $\bar{\sigma}_{ij}$ of a given m_f sublevel belonging to a particular composite level is defined as σ_{ij}/g_i, where g_i is the m_f degeneracy of the lower composite level of the $i\rightarrow j$ transition. Since the cross sections $\bar{\sigma}_{ij}$ and the level populations appearing in Eq. (12) involve narrow Lorentzians of widths no more than a few megahertz, the velocity integration limits can be safely taken from $-\infty$ to $+\infty$. With this assumption the velocity integration can be carried out without much difficulty. Further, Eq. (12) represents 20 integrals since N_1 and N_2 themselves involve five terms each [see Eqs. (7) and (8)]. Out of these, four integrals represent the probe absorption under unpumped conditions and set the base line for probe transmission in the neighborhood of a narrow resonance. Out of the remaining integrals, four represent the Lamb dip transitions corresponding to $i=1,2\rightarrow j=4,5$ absorptions due to atomic groups with nearly zero axial velocity. The remaining 12 integrals give rise to only 5 distinct crossover resonances at $\nu_0-\nu_1$, $\nu_0-\nu_2$, ν_0, $\nu_0+\nu_2$, and $\nu_0+\nu_1$ (see Fig. 2). A crossover resonance takes place when the laser frequency lies halfway between the hyperfine levels. Figure 3 shows one set of transitions responsible for the crossover resonance observed at ν_0. The pump at ν_0 appears downshifted to velocity group $+v_0$ of level 2. These atoms undergo an $i=2\rightarrow j=4$ transition at $\nu_0-\nu_1-\nu_2$. The same pump appears upshifted to the $-v_0$ velocity group of level 1 and causes an $i=1\rightarrow j=5$ transition at $\nu_0+\nu_1+\nu_2$. These transitions create small population bumps in levels 4 and 5 and similar bumps are also created in the populations of $-v_0$ group of level 2 and $+v_0$ group of level 1. The counterpropagating probe with a Doppler shift in the sense opposite

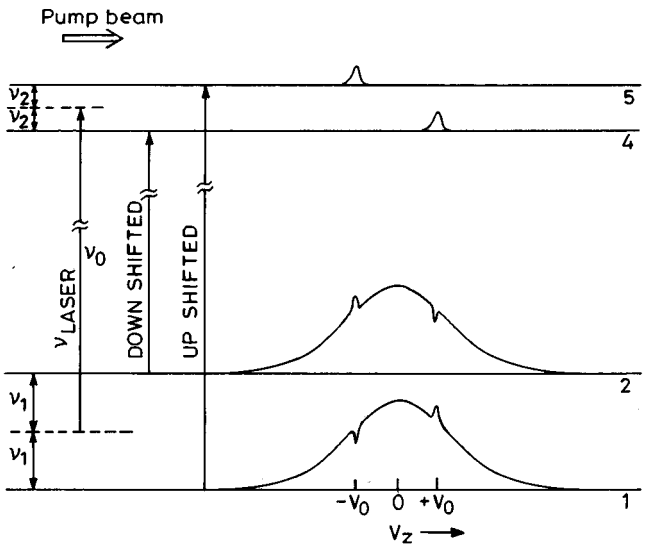

FIG. 3. One set of transitions responsible for the crossover resonance when $\nu_{\text{Laser}}=\nu_0$. Corresponding population changes among the composite levels are also shown.

to that of the pump finds enhanced absorption for these particular velocity groups. Similarly, it can be argued that the probe encounters increased absorption for the crossover resonances observed at $\nu_0-\nu_2$ and $\nu_0+\nu_2$ and reduced absorption for the resonances observed at $\nu_0-\nu_1$ and $\nu_0+\nu_1$. The population changes created by these transitions are monitored by the counterpropagating probe. The following expressions are obtained for the frequency-integrated probe absorption coefficients by once again extending the integration limits from $-\infty$ to $+\infty$:

$$\mathscr{A}_1(\nu=\nu_0-\nu_1-\nu_2)=-\frac{25}{12\times 24}S_0\frac{\left(-T\Gamma_{42}+2+\frac{T}{\tau}\right)}{\sqrt{1+S_{24}}}N_{2,0}, \tag{13}$$

$$\mathscr{A}_2(\nu=\nu_0-\nu_1+\nu_2)=-\frac{25}{12\times 24}S_0\frac{\left(-T\Gamma_{52}+2+\frac{T}{\tau}\right)}{\sqrt{1+S_{25}}}N_{2,0}, \tag{14}$$

$$\mathscr{A}_3(\nu=\nu_0+\nu_1-\nu_2)=-\frac{1}{9\times 18}S_0\frac{\left(-T\Gamma_{41}+2+\frac{T}{\tau}\right)}{\sqrt{1+S_{14}}}N_{1,0}, \tag{15}$$

$$\mathscr{A}_4(\nu=\nu_0+\nu_1+\nu_2)=-\frac{25}{9\times 18}S_0\frac{\left(-T\Gamma_{51}+2+\frac{T}{\tau}\right)}{\sqrt{1+S_{15}}}N_{1,0}, \tag{16}$$

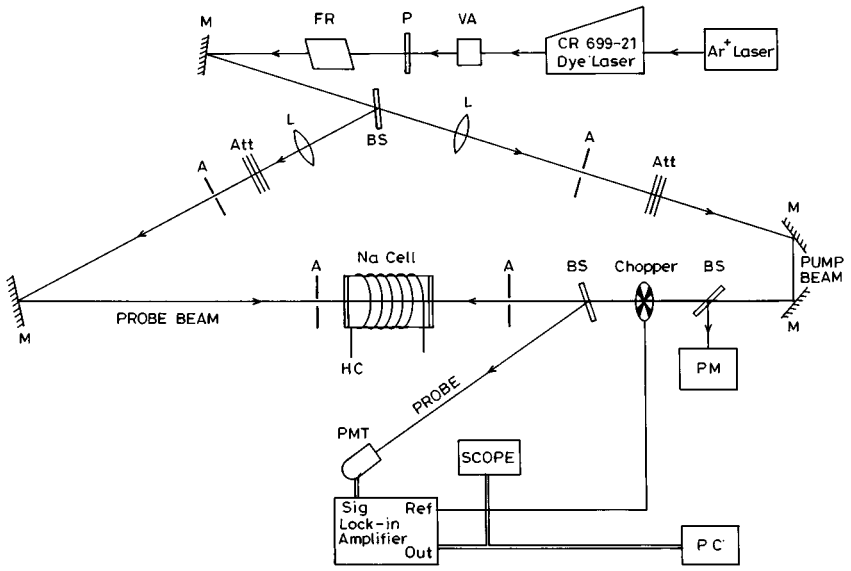

FIG. 4. Experimental setup for VSOP. VA, variable attenuator; P, linear polarizer; FR, Fresnel rhomb; M, mirror; BS, beam splitter; L, lens; A, aperture; Att, neutral density filters; HC, heater coil; PM, power meter; PMT, photomultiplier tube; PC, personal computer. Other experimental conditions are stated in the text.

$$\mathscr{A}_5(\nu=\nu_0-\nu_1)=\frac{\left(1+\frac{T}{\tau}-T\Gamma_{42}\right)}{\left(2+\frac{T}{\tau}-T\Gamma_{42}\right)}\mathscr{A}_1 + \frac{\left(1+\frac{T}{\tau}-T\Gamma_{52}\right)}{\left(2+\frac{T}{\tau}-T\Gamma_{52}\right)}\mathscr{A}_2, \tag{17}$$

$$\mathscr{A}_6(\nu=\nu_0-\nu_2)=\frac{4}{15}\frac{(1-T\Gamma_{41})}{\left(2+\frac{T}{\tau}-T\Gamma_{42}\right)}\mathscr{A}_1 + \frac{15}{4}\frac{(1-T\Gamma_{42})}{\left(2+\frac{T}{\tau}-T\Gamma_{41}\right)}\mathscr{A}_3, \tag{18}$$

$$\mathscr{A}_7(\nu=\nu_0)=\frac{4}{3}\frac{(-T\Gamma_{41})}{\left(2+\frac{T}{\tau}-T\Gamma_{42}\right)}\mathscr{A}_1 + \frac{4}{15}\frac{(-T\Gamma_{51})}{\left(2+\frac{T}{\tau}-T\Gamma_{52}\right)}\mathscr{A}_2 + \frac{15}{4}\frac{(-T\Gamma_{42})}{\left(2+\frac{T}{\tau}-T\Gamma_{41}\right)}\mathscr{A}_3 + \frac{3}{4}\frac{(-T\Gamma_{52})}{\left(2+\frac{T}{\tau}-T\Gamma_{51}\right)}\mathscr{A}_4, \tag{19}$$

$$\mathscr{A}_8(\nu=\nu_0+\nu_2)=\frac{4}{3}\frac{(1-T\Gamma_{51})}{\left(2+\frac{T}{\tau}-T\Gamma_{52}\right)}\mathscr{A}_2 + \frac{3}{4}\frac{(1-T\Gamma_{52})}{\left(2+\frac{T}{\tau}-T\Gamma_{51}\right)}\mathscr{A}_4, \tag{20}$$

$$\mathscr{A}_9(\nu=\nu_0+\nu_1)=\frac{5}{1}\frac{\left(1+\frac{T}{\tau}-T\Gamma_{41}\right)}{\left(2+\frac{T}{\tau}-T\Gamma_{51}\right)}\mathscr{A}_3 + \frac{1}{5}\frac{\left(1+\frac{T}{\tau}-T\Gamma_{51}\right)}{\left(2+\frac{T}{\tau}-T\Gamma_{51}\right)}\mathscr{A}_4, \tag{21}$$

where

$$S_0=\frac{\sqrt{\pi}I\tau_e(\pi\lambda\!\!\!^{-2}\gamma_n)^2}{8kuh\nu} \tag{22}$$

and $1/\tau_e=1/\tau+1/T$, $\gamma_n=1/\tau$, and $\lambda\!\!\!^{-}=\lambda/2\pi$ where λ is the wavelength of the transition in question. $\mathscr{A}_1$–$\mathscr{A}_4$ give the frequency-integrated absorption coefficients for the Lamb dips LD_1–LD_4 and $\mathscr{A}_5$–$\mathscr{A}_9$ are the corresponding quantities for the crossover resonances CR_5–CR_9.

IV. EXPERIMENTAL DETAILS

We have used the technique of velocity-selective optical pumping (VSOP) to record transitions among the hyperfine levels of the sodium $D1$ line. Figure 4 shows schematically the experimental configuration. A cylindrical Pyrex cell of length 10 cm and diameter 2.5 cm was filled with distilled sodium vapor. No buffer gas was used. The ends of the cell were heated differentially to avoid Na vapor deposition on the windows. The cell temperature could be varied up to

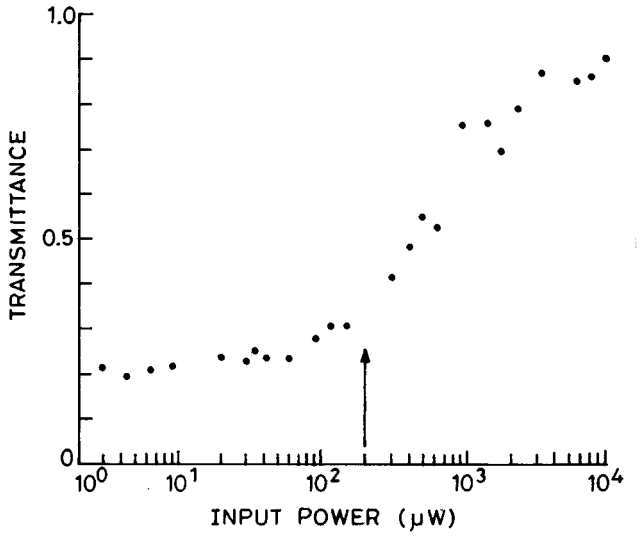

FIG. 5. Saturation characteristics for the Na $D1$ transition at 150 °C. The arrow indicates the operating power point in our experiments.

180 °C. However, measurements were made at 115 °C, 120 °C, 147 °C, and 169 °C as recorded by a thermocouple. The actual vapor temperatures may be somewhat lower. The counterpropagating pump and the probe beams having the same sense of circular polarization were derived from the same single-mode cw tunable ring dye laser, Coherent model 699-21. The effective laser bandwidth was of the order of 1–2 MHz. The beams were expanded by a long focal length lens so that the pump and the probe diameters over the length of the cell were nearly 5 mm and 2 mm respectively. A Fresnel rhomb was used to circularly polarize the laser beam. The pump and the probe powers throughout these experiments were kept at 200 μW and 1 μW, respectively. These values correspond to pump and probe intensities in the cell to be around 10 μW/mm^2 and 0.3 μW/mm^2 respectively. Figure 5 shows that at this pump power, the saturation effects are just begining to show up. Therefore, the saturation and coherent effects, if present in our experiment, are unlikely to be dominant. The probe transmission is recorded by the lock-in-detection method with the pump chopped at 389 Hz. Because of the variation in the signal level of various resonances, different lock-in sensitivities had to be used in the three significant regions. The recorded resonances at the cell temperature of 120 °C and beam conditions as specified above are shown in Figs. 6(a)–6(c). We have also measured the relaxation time T. For this measurement, the pump beam was chopped by an A-O modulator, modulated at 1 kHz by an external function generator. The signal decay was recorded over several repeated runs with the help of a boxcar integrator and subsequently stored in a personal computer (PC). An exponential fit to the data is shown in Fig. 7. The pump pulse decay under identical experimental conditions is shown in the inset. Whereas the pump pulse decay constant is about 0.4 μsec, the signal decay constant and hence the relaxation time is of the order of 3.2 μsec. The spatial profile of the VSOP signal was also measured by displacing the pump beam parallel to the fixed probe. Figure 8 shows such a profile at 0.4 mW and 50 mW pump powers while the probe beam was held at 1 μW.

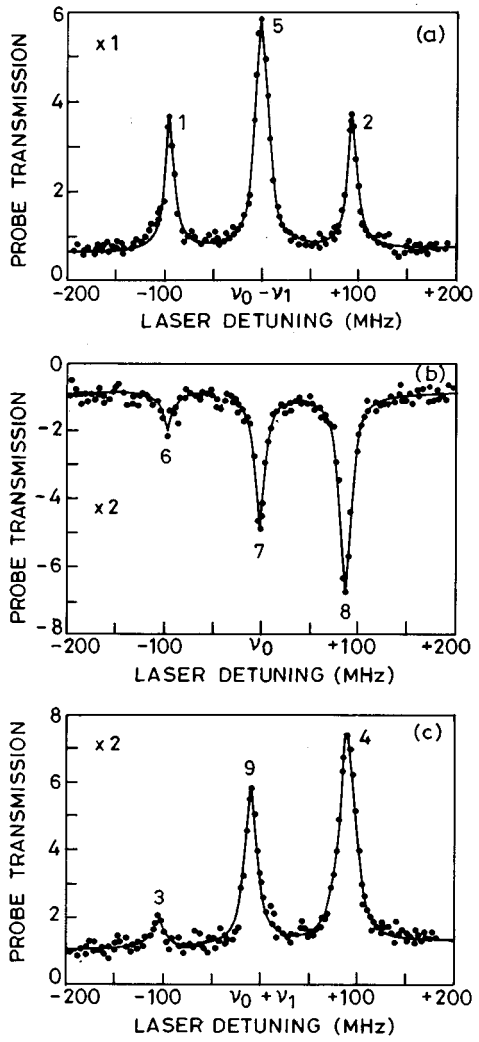

FIG. 6. Lamb dips and crossover resonances of the ^{23}Na $D1$ line recorded at 120 °C with $I_{\text{pump}}=10$ μW/mm^2 while $I_{\text{probe}}=0.3$ μW/mm^2. Peaks 1–4 are the Lamb dips LD_1–LD_4 whereas peaks 5–9 are the crossovers CR_5–CR_9. (a) Transitions $F_g=2\rightarrow F_e=1,2$. (b) Transitions $F_g=1,2\rightarrow F_e=1$; $F_g=1,2\rightarrow F_e=1,2$; and $F_g=1,2\rightarrow F_e=2$. (c) Transitions $F_g=1\rightarrow F_e=1,2$.

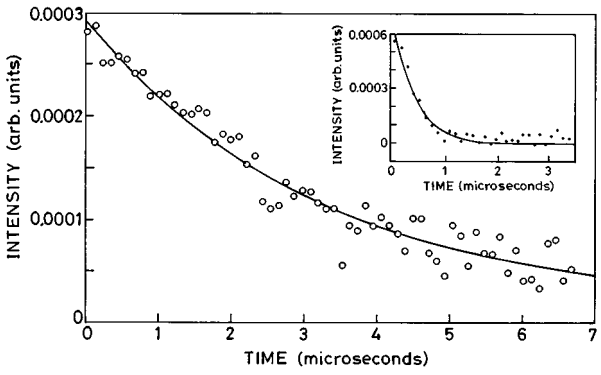

FIG. 7. Probe signal decay subsequent to the pump switch off plotted to obtain the relaxation time T. The inset shows the pump pulse decay. The pump and the probe beams are both coincident.

V. RESULTS AND DISCUSSION

All quantities appearing in expressions (13)–(21) for the frequency-integrated absorption coefficients for the Lamb dips and the crossover resonances are, in principle, known. The excited-state lifetime τ is known to be 16.4 nsec [1] and the decay rates Γ_{ji} are calculated by Quivers's [5] and are given in Table I. The relaxation time T, in the present case, is measured to be 3.2 μsec. One could check the validity of the five level model by comparing the calculated absorption coefficients of the narrow resonances with those observed experimentally or, alternatively, one could obtain experimental values of the atomic cross sections from the measured areas under the resonances. However, we have decided to check the five-level model through relations (17)–(21), which relate the theoretical absorption coefficients of the crossover resonances with those of the Lamb dips. Under our experimental conditions, with $T/\tau \gg 1$, the above expressions get simplified to

$$\mathscr{A}_5 = \mathscr{A}_1 + \mathscr{A}_2, \tag{23}$$

$$\mathscr{A}_6 = -\frac{3}{1}\mathscr{A}_3 - \frac{2}{15}\mathscr{A}_1, \tag{24}$$

$$\mathscr{A}_7 = -\frac{16}{75}\mathscr{A}_2 - \frac{2}{3}\mathscr{A}_1 - \frac{9}{16}\mathscr{A}_4 - \frac{3}{1}\mathscr{A}_3, \tag{25}$$

$$\mathscr{A}_8 = -\frac{16}{15}\mathscr{A}_2 - \frac{9}{16}\mathscr{A}_4, \tag{26}$$

$$\mathscr{A}_9 = \frac{5}{1}\mathscr{A}_3 + \frac{1}{5}\mathscr{A}_4. \tag{27}$$

It is immediately realized that the crossover resonance areas $\mathscr{A}_6, \mathscr{A}_7, \mathscr{A}_8 (\mathscr{A}_5, \mathscr{A}_9)$ have signs opposite (the same as) those of the Lamb dip areas. The following argument makes this plausible. The Lamb dips correspond to reduced probe absorption as the pump transfers zero velocity atoms from levels 1 and 2 to the pumped level 3. For the $\mathscr{A}_5$ crossover resonance, the pump burns holes in the $+v_0$ and $-v_0$ velocity groups in the ground-state level 2 and the counterpropagating probe absorption is therefore reduced. The same argument holds for the $\mathscr{A}_9$ crossover. As discussed in Sec. III, the probe transmission for $\mathscr{A}_6$, $\mathscr{A}_7$, and $\mathscr{A}_8$ resonances, on the other hand, decreases. Before we begin to verify the results (23)–(27), it must be realized that experimentally we measure the change in the transmitted probe intensity and not directly the change in the absorption coefficient. If $I_t(0)$ and $I_t(p)$ represent respectively the transmitted intensities in the absence and presence of the pump and $\alpha(0)$ and $\alpha(p)$ are the corresponding absorption coefficients, and if further $\alpha(0)L \ll 1$ and $\alpha(p)L \ll 1$, where L is the cell length, then the change in the transmitted intensity is proportional to the change in the absorption coefficient

$$I_t(p) - I_t(0) = I_0[\alpha(0)L - \alpha(p)L]. \tag{28}$$

Here I_0 is the incident probe intensity. Under these conditions, which are definitely satisfied at 120 °C with $\alpha(0)L = 0.16$, we can directly compare the areas under the resonances. Table II lists the areas under the resonances as obtained from the Lorentzians fitted to the line profiles recorded at 120 °C. We notice that the Lamb dip LD_3 with area $\mathscr{A}_3$ corresponding to the 1-4 transition is nearly an order of magnitude weaker than the other Lamb dips. Similar observation has been made by Nakayama [8]. Further, the crossover resonance CR_6 with area $\mathscr{A}_6$, which is the first crossover resonance with increased absorption, is also rather weak. To make internal checks on the predictions of the five-level model, we have compared in Table III the measured areas of the crossover resonances with those calculated from the measured Lamb dip areas [Eqs. (23)–(27)]. The agreement for the resonances CR_5 and CR_9 (the crossover resonances between each pair of Lamb dip resonances) is excellent. These resonances correspond to the pump and the probe beams interacting with only one of the ground hyperfine levels. The crossover resonance CR_5 and the assosciated Lamb dips LD_1 and LD_2 are recorded in a continuous laser scan; consequently we do not expect any experimental uncertainities in their relative areas. The same holds for the crossover resonance CR_9. However, the same cannot be said about CR_6–CR_8 crossover resonances because being sufficiently far away from either pair of Lamb dips, the experimental

TABLE II. Areas under narrow resonances (at 120 °C).

Resonance[a]	Area (arbitrary units)
LD1	4.5×10^{-5}
LD2	5.2×10^{-5}
LD3	5.3×10^{-6}
LD4	6.4×10^{-5}
CR5	9.7×10^{-5}
CR6	-5.0×10^{-6}
CR7	-2.2×10^{-5}
CR8	-3.8×10^{-5}
CR9	3.8×10^{-5}

[a]LD1–LD4 are Lamb dips and CR5–CR9 are crossover resonances.

TABLE III. Verification of the predictions of the five level model (at 120 °C).

Measured areas of the crossover resonances (arbitrary units)	Areas of the crossover resonances as obtained from Lamb dip areas (arbitrary units)
$\mathscr{A}_5$ 9.7×10^{-5}	$\mathscr{A}_1+\mathscr{A}_2$ 9.7×10^{-5}
$\mathscr{A}_6$ -5.0×10^{-6}	$-\frac{2}{15}\mathscr{A}_1-3.\mathscr{A}_3$ -2.0×10^{-5}
$\mathscr{A}_7$ -2.2×10^{-5}	$-\frac{2}{3}\mathscr{A}_1-\frac{16}{75}\mathscr{A}_2-3.\mathscr{A}_3-\frac{9}{16}\mathscr{A}_4$ -9.3×10^{-5}
$\mathscr{A}_8$ -3.8×10^{-5}	$-\frac{16}{15}\mathscr{A}_2-\frac{9}{16}\mathscr{A}_4$ -8.9×10^{-5}
$\mathscr{A}_9$ 3.8×10^{-5}	$5.\mathscr{A}_3+\frac{1}{5}\mathscr{A}_4$ 4.0×10^{-5}

TABLE IV. Linewidths of narrow resonances.

Resonance	FWHM (MHz) at 115 °C	FWHM (MHz) at 169 °C
LD1	16±2	11±2
LD2	14±1	8.5±.7
LD3	[a]	12±2
LD4	16±1	7±1
CR5	14±1	8±1
CR6	16±2	13±1
CR7	15±1	15±1
CR8	16±1	17±0.1
CR9	14±3	9.3±0.8

[a]Too weak.

condition may have changed somewhat despite our best efforts to keep them the same. We observe that in Eqs. (23)–(27), the area $\mathscr{A}_3$ of the LD_3 resonance is getting multiplied by comparatively larger numerical factors and any uncertainity in the measurement of its area is going to adversely affect our comparison. This is further compounded by the fact that the signal-to-noise ratio for this Lamb dip is the worst among all resonances. However, we do not think that the large discrepancies (a factor of 4 for the CR_6 and CR_7 resonances and factor of 2 for the CR_8 resonance) observed are due to experimental uncertainties. We have repeated measurements under varying experimental conditions, but we have always found excellent agreement for CR_5 and CR_9 and similar disagreement for the remaining cross-over resonances. It should be noted that the CR_6, CR_7, and CR_8 resonances are more complex as the pump simultaneously creates population changes in both ground-state hf levels and the probe also simultaneously interacts with both ground-state hf levels.

VI. LINEWIDTHS

Narrow resonances were recorded repeatedly under similar conditions. Except in a few cases such as the Lamb dip LD_2, the recorded line profiles are quite symmetrical. They were fitted to single Lorentzians by a fitting routine on the PC. The solid lines in Figs. 6(a)–(c) are the calculated Lorentzian profiles. Table IV lists the mean linewidths (FWHM) and the standard deviations of all nine resonances recorded at 115 °C and 169 °C. The slight power broadening at 115 °C is substantially reduced at 169 °C. Under unpumped conditions, the cell absorption of 11% at 115 °C gives a low-power attenuation constant $\alpha_0 L = 0.11$; with 96% absorption at 169 °C, the corresponding constant $\alpha_0 L = 3.2$. We did not record resonances at still higher temperatures. The 16.4-nsec lifetime of the $D1$ transition corresponds to a natural linewidth of about 9.7 MHz. We notice that at 169 °C, the linewidths of most of the resonances fall in the range of natural widths. The Lamb dips LD_2 and LD_4 and the crossover resonances CR_5 and CR_9 seem to show subnatural linewidths.

VII. SPATIAL PROFILE STUDIES

Before we conclude, we would like to discuss the results of our measurments on the distribution of oriented atoms in the cell. The atoms in the selected velocity groups get oriented within the interaction volume by the optical pumping process and begin to diffuse towards the cell walls. It is therefore possible to detect such atoms even when the probe beam is displaced away from the pump beam. The spatial profiles of the oriented atoms shown in Fig. 8 were obtained by recording the probe transmission after locking the single-mode laser near the peak of a particular narrow resonance and moving the pump beam across the fixed probe beam. The presence of the noise in the measured profiles is due to the faulty mirror drive arrangement. However, it is certain that the spatial profile at 50-mW pump power is not narrower than the one recorded at 0.4 mW. The oriented atoms (atoms in the composite level 3) do not absorb the pump photons as mentioned earlier, but can lose their orientation by absorbing the fluorescence photons, which have random states of polarization. The probability of the emitted photons being reabsorbed by the oriented atoms increases at higher pump powers because of the increased availability of such photons. This gives rise to the narrowing of the spatial profile at higher pump powers, as reported in the literature [9]. However, no narrowing of the spatial profile was observed by us because the number of oriented atoms is quite small in our buffer-free experiments. The narrow-band laser is able to orient a very small fraction of the atoms unless a buffer gas is used, which spreads the orientation to the entire Doppler profile via velocity-changing collisions. Our narrow resonance signals are essentially against a flat background, suggesting the absence of pedestal effects, which are produced by the VCC's. This justifies our neglect of collision terms in the rate equations.

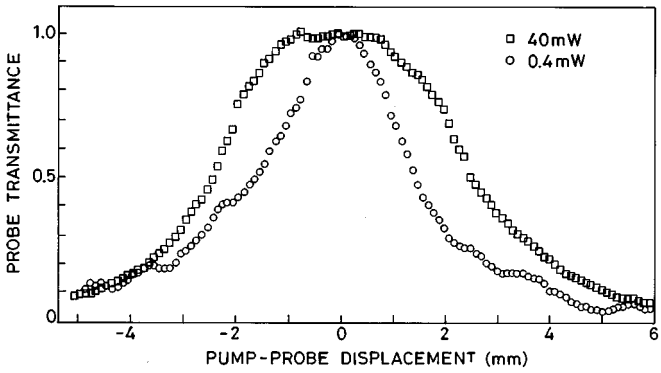

FIG. 8. Normalized transmitted probe signal as a function of pump-probe displacement for various pump powers. Pump beam: □, 40 mW; O, 0.4 mW. Probe: 1 μW in both cases.

VIII. CONCLUSION

We have recorded Lamb dip and crossover resonances for the sodium $D1$ transition in a 10-cm cell by the technique of velocity-selective optical pumping. In view of the complexity of the sodium $D1$ transition, it was decided not to use any buffer gas in the initial stage so that the theoretical model could be tested without the use of free parameters. We have applied Quivers's five-level model to interpret the experimental results. The rate equation description, rather than the density-matrix approach, was adopted to obtain steady-state population changes caused by a relatively weak pump of

200-μW power. Within this approach, the frequency-integrated absorption coefficients of all crossover resonances can be expressed in terms of the frequency-integrated absorption coefficients of the Lamb dips. It is found that such relations are fully satisfied in the case of crossover resonances that correspond to transitions starting from only one of the ground hyperfine levels. However, there are substantial disagreements for the crossover resonances where both the ground hyperfine levels are involved. Any coherence effects, if present, are more likely to show up for these resonances. Theoretically such effects are predicted in three-level systems under weak pumping conditions as well [10]. However, it is gratifying to note that at 169 °C Doppler and power broadenings are considerably reduced in our experiment. Some lines show widths that may be just below the natural linewidth of 10 MHz.

APPENDIX

$$S_{14}=\frac{\sigma_{14}IT\tau_e}{12h\nu}\left(-4\Gamma_{41}+\frac{4}{\tau_e}+\frac{4}{T}\right), \tag{A1}$$

$$S_{15}=\frac{\sigma_{15}IT\tau_e}{12h\nu}\left(-4\Gamma_{51}+\frac{4}{\tau_e}+\frac{3}{T}\right), \tag{A2}$$

$$S_{24}=\frac{\sigma_{24}IT\tau_e}{12h\nu}\left(-3\Gamma_{42}+\frac{3}{\tau_e}+\frac{4}{T}\right), \tag{A3}$$

$$S_{25}=\frac{\sigma_{25}IT\tau_e}{12h\nu}\left(-3\Gamma_{52}+\frac{3}{\tau_e}+\frac{3}{T}\right), \tag{A4}$$

$$S_{14}^{1}=\frac{T\tau_e}{12}\left[\frac{\sigma_{14}I}{h\nu}\left(\frac{4N_1^0}{T}\right)-\frac{12N_1^0}{T\tau_e}S_{14}\right], \tag{A5}$$

$$S_{15}^{1}=\frac{T\tau_e}{12}\left[\frac{\sigma_{15}I}{h\nu}\left(\frac{3N_1^0}{T}\right)-\frac{12N_1^0}{T\tau_e}S_{15}\right], \tag{A6}$$

$$S_{24}^{1}=\frac{T\tau_e}{12}\left[\frac{\sigma_{24}I}{h\nu}\left(\frac{4N_1^0}{T}+3\Gamma_{41}N_2^0-3\Gamma_{42}N_1^0+\frac{3N_1^0}{\tau_e}\right)-\frac{12N_1^0}{T\tau_e}S_{24}\right], \tag{A7}$$

$$S_{25}^{1}=\frac{T\tau_e}{12}\left[\frac{\sigma_{25}I}{h\nu}\left(\frac{3N_1^0}{T}+3\Gamma_{51}N_2^0-3\Gamma_{52}N_1^0+\frac{3N_1^0}{\tau_e}\right)-\frac{12N_1^0}{T\tau_e}S_{25}\right], \tag{A8}$$

$$S_{14}^{2}=\frac{T\tau_e}{12}\left[\frac{\sigma_{14}I}{h\nu}\left(\frac{4N_2^0}{T}+4\Gamma_{42}N_1^0-4\Gamma_{41}N_2^0+\frac{4N_2^0}{\tau_e}\right)-\frac{12N_2^0}{T\tau_e}S_{14}\right] \tag{A9}$$

$$S_{15}^{2}=\frac{T\tau_e}{12}\left[\frac{\sigma_{15}I}{h\nu}\left(\frac{3N_2^0}{T}+4\Gamma_{52}N_1^0-4\Gamma_{51}N_2^o+\frac{4N_2^0}{\tau_e}\right)-\frac{12N_2^0}{T\tau_e}S_{15}\right] \tag{A10}$$

$$S_{24}^{2}=\frac{T\tau_e}{12}\left[\frac{\sigma_{24}I}{h\nu}\left(\frac{4N_2^0}{T}\right)-\frac{12N_2^0}{T\tau_e}S_{24}\right], \tag{A11}$$

$$S_{25}^{2}=\frac{T\tau_e}{12}\left[\frac{\sigma_{25}I}{h\nu}\left(\frac{3N_2^0}{T}\right)-\frac{12N_2^0}{T\tau_e}S_{25}\right], \tag{A12}$$

$$S_{14}^{4}=\frac{T\tau_e}{12}\,4\frac{\sigma_{14}I}{h\nu}\left(\frac{N_1^0}{T}\right), \tag{A13}$$

$$S_{24}^{4}=\frac{T\tau_e}{12}\,3\frac{\sigma_{24}I}{h\nu}\left(\frac{N_2^0}{T}\right), \tag{A14}$$

$$S_{15}^{5}=\frac{T\tau_e}{12}\,\frac{\sigma_{15}I}{h\nu}\left(4\frac{N_1^0}{T}\right), \tag{A15}$$

$$S_{25}^{5}=\frac{T\tau_e}{12}\,\frac{\sigma_{25}I}{h\nu}\left(3\frac{N_2^0}{T}\right), \tag{A16}$$

$$\frac{1}{\tau_e}=\frac{1}{T}+\frac{1}{\tau}. \tag{A17}$$

[1] T.W. Hänsch, I.S. Shahin, and A.L. Schawlow, Phys. Rev. Lett. **27**, 707 (1971).
[2] C. Wieman and T.W. Hänsch, Phys. Rev. Lett. **36**, 1170 (1976).
[3] M. Pinard, C.G. Aminoff, and F. Laloë, Phys. Rev. A **19**, 2366 (1979).
[4] P.G. Pappas, R.A. Forber, W.W. Quivers, Jr., R.R. Dasari, M.S. Feld, and D.E. Murnik, Phys. Rev. Lett. **47**, 236 (1981).
[5] W.W. Quivers, Jr., Phys. Rev. A **34**, 3822 (1986).
[6] S. Svanberg, G.-Y. Yan, T.P. Duffey, W.-M. Du, T.W. Hänsch, and A.L. Schawlow, J. Opt. Soc. Am. B **4**, 462 (1987).
[7] G. Shimkaveg, W.W. Quivers, Jr., R.R. Dasari, and M.S. Feld, Phys. Rev. A **48**, 1409 (1993).
[8] Shigeru Nakayama, J. Opt. Soc. Am. B **2**, 1431 (1985).
[9] G. Ankerhold, M. Schiffer, D. Mutschall, T. Scholz, and W. Lange, Phys. Rev. A **48**, R4031 (1993).
[10] G. Orriols, Nuovo Cimento B **53**, 1 (1979).